Wireless Multifunctional Surface Acoustic Wave Sensor for Magnetic Field and Temperature Monitoring

Yang Yang, Prince Mengue, Harshad Mishra, Cécile Floer, Sami Hage-Ali, S. Petit-Watelot, Daniel Lacour, Michel Hehn, Tao Han, Omar Elmazria

ADVANCED MATERIALS TECHNOLOGIES
www.advmattechnol.de

Wireless Multifunctional Surface Acoustic Wave Sensor for Magnetic Field and Temperature Monitoring

Yang Yang, Prince Mengue, Harshad Mishra, Cécile Floer, Sami Hage-Ali, Sébastien Petit-Watelot, Daniel Lacour, Michel Hehn, Tao Han, and Omar Elmazria*

A one-port surface acoustic wave (SAW) resonator based on Co_{40}–Fe_{40}–B_{20}/SiO_2/ZnO/quartz multilayer structure and exhibiting a dual mode, Rayleigh and Love wave modes, is investigated to achieve a multifunctional sensor measuring both temperatures and magnetic fields. The Rayleigh wave mode of the resonator is used for temperature measurement with a temperature sensitivity of −37.9 ppm/°C, and the Love wave mode is used for magnetic field measurement. Co_{40}-Fe_{40}-B_{20} is the magnetic sensitive layer, and quartz crystal is the piezoelectric substrate. ZnO film is also a piezoelectric but considered here in combination with SiO_2 as insulating layers and serves to control impedance matching and temperature dependence of the sensor. ZnO and SiO_2 thicknesses are selected to realize temperature compensation for the Love wave mode and making this mode highly sensitive to magnetic fields and insensitive to temperatures. The magnetic field sensitivities of −170.4 kHz m^{-1} T^{-1} and −621.6 kHz m^{-1} T^{-1} are obtained respectively for the fundamental and the third harmonic of the Love wave mode. The proposed structure is beneficial to design reliable hybrid SAW magnetic field and temperature sensors.

1. Introduction

The developments of magnetic field sensors generate a wide range of applications, such as: magnetoencephalography, magnetic resonance imaging in biomedical field, rotational sensors, magnetic anomaly detection for automotive, magnetic switches, and measurement of electric currents. Recent developments in the field of the Internet of Things (IoT), the factory of the future (Industry 4.0) and autonomous vehicles have generated new needs for wireless magnetic sensors with low energy consumption or even passive (batteryless). For example, wireless magnetic sensors are designed to detect magnetic anomaly and are used for street installation, traffic control, and detection of the parking space availability. The sensor responds to changes in the earth's magnetic field caused by the presence of a vehicle, generally a metallic structure. Installation would be easier and cost-effective if the sensors are batteryless and could be installed into the asphalt or pavement (i.e., buried), thereby eliminating the risk of degradation and the need for regular maintenance, particularly the change of batteries. Another application example for wireless magnetic sensors concerns remote electric current sensing including transient-state electric currents on overhead power lines. Indeed, the development of smart grids requires the development of reliable and low-cost sensor networks. Monitoring electric currents at present and especially in medium and high voltage power lines is difficult and expensive when installing conventional sensors.[1,2] The indirect measurement of electric currents through the generated magnetic fields is an elegant solution. The sensor must also be insensitive to the temperature of the wire that strongly depends on the electric current flowing.

Surface acoustic wave (SAW) devices are key components in communication systems and are widely used as filters, delay lines or resonators. They are still relevant for the development of 5G compatible technologies.[3,4] Because SAW devices are highly sensitive to physical parameters that affect SAW velocities, they also offer promising solutions as sensors in a wide range of applications.[5–8] SAW sensors have the advantage of being micro, passive, wireless, and even packageless in specific configurations.[9–12] SAW sensor technology allows simultaneous and independent measurement of temperatures and magnetic fields (i.e., electric current). SAW devices based on ferromagnetic films have been studied for the development of magnetic field and electric current sensors.[13–28] However, the environment temperature is a factor affecting the performance of SAW sensors. An unavoidable fact is that SAW magnetic field sensors without temperature compensation are sensitive to both magnetic fields and temperatures due to the negative temperature coefficients of ferromagnetic films.[26,29] It leads to a difficulty in discrimination between them or their simultaneous measurement. Therefore, a SAW sensor that measures

Y. Yang, T. Han
School of Electronic Information and Electrical Engineering
Shanghai Jiao Tong University
Shanghai 200240, China
P. Mengue, H. Mishra, C. Floer, S. Hage-Ali, S. Petit-Watelot, D. Lacour, M. Hehn, O. Elmazria
The Institut Jean Lamour UMR 7198
Université de Lorraine – CNRS
Nancy 54000, France
E-mail: omar.elmazria@univ-lorraine.fr
The ORCID identification number(s) for the author(s) of this article can be found under https://doi.org/10.1002/admt.202100860.

DOI: 10.1002/admt.202100860

magnetic fields and temperatures simultaneously is required. An integrated single chip SAW sensor with the capability of measuring magnetic fields and temperatures based on two delay line structures has been reported.[29] However, the wireless aspect is not considered, and the effect of temperatures on the sensitivity of the sensor is often neglected.

In this study, a magnetic field and temperature multifunctional SAW sensor is developed based on a one-port dual mode Co_{40}–Fe_{40}–B_{20}/SiO_2/ZnO/Al/quartz resonator. The sensor has Rayleigh wave mode for temperature measurement and Love wave mode for magnetic field measurement. This structure allows flexibility of film thickness choice for temperature compensation and exhibits a weak hysteresis along the hard axis. A near zero temperature coefficient of frequency (TCF) of the Love wave mode is obtained due to the combined negating thermal effects of the different films. The impedance matching and the quality factor are carefully considered. The scattering parameters of the SAW sensor change slightly with temperature which is an advantage in the operation of the sensor in real applications. The magneto-acoustic response of the device is measured versus various magnetic fields. The sensor is tested in a wireless demonstration in a DC electric current scenario.

2. Design and Fabrication

Based on theoretical finite element multi-physics coupling calculations,[30] synchronous single-port SAW resonators are fabricated to operate around the ISM band at 433 MHz and to exhibit a high sensitivity to magnetic field and almost zero TCF for Love wave mode. A one-port resonator can be connected to an antenna as a wireless and passive sensor, which is an advantage of a one-port resonator. Thus, using photolithography and a lift-off based fabrication process, SAW resonators are fabricated with 100 nm thick aluminum electrodes on ST-cut quartz, propagation along X+90°. The spatial period of the interdigital transducers (IDT) is set to 10 µm fixing thus the wavelength of the device ($\lambda = 10$ µm). The pitch of IDT electrodes is the same with that of electrode reflectors. The aperture is fixed to 40 λ.

To realize the resonator with a zero TCF, 0.03λ thick zinc oxide (ZnO) film is sputtered overlaying the IDTs on the quartz substrate, followed by a deposition of 0.025λ thick silica (SiO_2) film over the ZnO. The contact pads are protected by photoresist during the depositions to allow characterization in the subsequent stages. The magnetic sensitive layer (Co–Fe–B) is then deposited on the top of the structure as sketched in **Figure 1**.

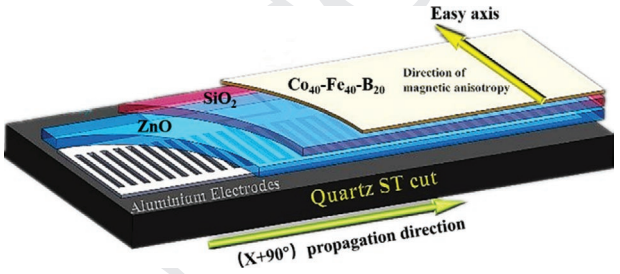

Figure 1. Schematic illustration of the structure of the fabricated device with wave propagation along (X+90°) and easy axis of ferromagnetic layer (Co–Fe–B) parallel to X direction.

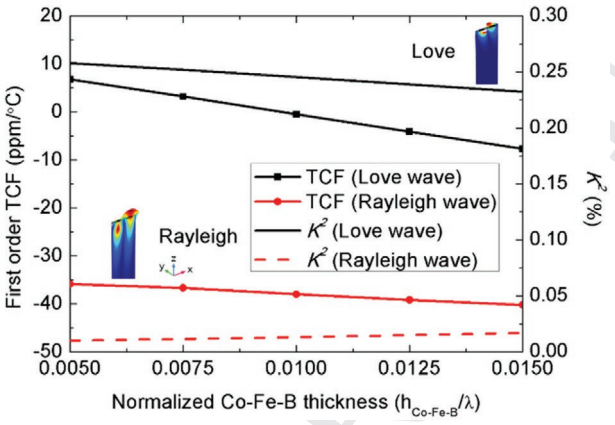

Figure 2. The calculated TCF and electromechanical coupling coefficient variations of Love wave and Rayleigh wave modes on Co–Fe–B/SiO_2/ZnO/ST+90° -cut quartz as a function of Co–Fe–B thicknesses.

The first-order TCF and electromechanical coupling coefficient variations of the Love wave and Rayleigh wave versus the Co–Fe–B thicknesses in a single resonator are illustrated in **Figure 2**. The TCF simulations are performed by taking consideration of the thermal stress, thermal strains, thermal expansion, temperature coefficients, and the third order material constants. The simulated TCF values of Love wave and Rayleigh wave modes decrease with adding Co–Fe–B thicknesses. A near zero TCF is obtained for the Love wave mode when the Co–Fe–B film is 0.01λ. The temperature compensated Love wave mode is used for magnetic field sensing. Meanwhile, the thermal sensitivity of the Rayleigh wave mode for temperature sensing is −37.9 ppm/°C. The electromechanical coupling coefficients for Love and Rayleigh wave modes are calculated by $K^2 = \pi f_r/(2f_a \cdot \tan(\pi f_r/2f_a))$. f_r is the resonance frequency, and f_a is the anti-resonance frequency. Rayleigh wave mode is not electrically excited on ZnO/ST+90°-cut Quartz and SiO_2/ZnO/ST+90°-cut Quartz. After depositing Co–Fe–B, Rayleigh wave mode is electrically excited. The resonance frequency of Love wave mode decreases due to the mass loading caused by the multilayers. The electromechanical coupling coefficient of the Love wave mode decreases with adding the Co–Fe–B thickness. In contrast, the electromechanical coupling coefficient of the Rayleigh wave mode increases slowly with Co–Fe–B thickness. The reflection coefficients of Love wave mode and Rayleigh wave mode are 0.098 and 0.034 respectively when the Co–Fe–B thickness is 100 nm. The synchronous resonator consists of 100 electrode pairs for IDT and 200 electrode reflectors on the both sides of IDTs, which are decided by the electromechanical coupling coefficient and reflection coefficient respectively.

A ferromagnetic Co_{40}–Fe_{40}–B_{20} thin film is used as the active layer for magnetic field sensing. This specific material is chosen to enable a sensitivity to low magnetic fields, thanks to its low intrinsic magnetic anisotropy. A 5 nm thick tantalum (Ta) buffer layer is first deposited over the SiO_2/ZnO/ST(X+90°) structure in order to improve the adhesion of the active layer. Then 100 nm thick Co_{40}–Fe_{40}–B_{20} layer is deposited by DC sputtering of a 2-inch target at 300 W and 5×10^{-3} mbar of Ar and capped with a 5 nm thick platinum (Pt) as a protective layer from contamination and oxidation. Taking consideration of

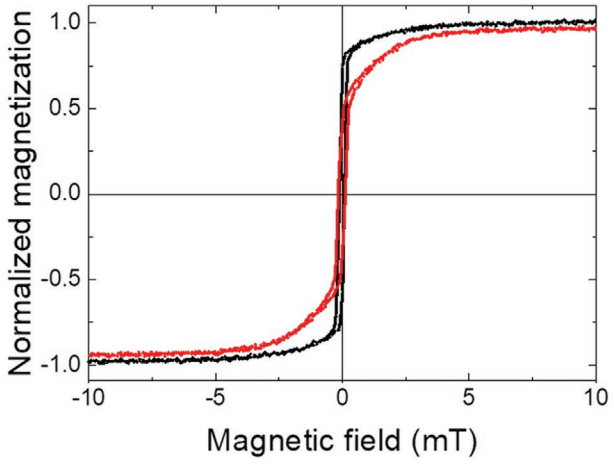

Figure 3. In-plane room temperature measured magnetization along the hard axis (red) and easy axis (black) of the Ta(5 nm)/Co_{40}–Fe_{40}–B_{20}(100 nm)/Pt(5 nm) deposited thin film layer.

anisotropy, damping loss, TCF, and sensitivity, the 100 nm thickness of Co_{40}–Fe_{40}–B_{20} layer is optimum to simultaneously exhibit a sensitivity to magnetic field and to prevent an out-of-plane component of magnetization. Indeed, out-of-plane component appears for thicker Co_{40}–Fe_{40}–B_{20} layers. Magnetic characterizations of the sample have been conducted using a Vibrating Sample Magnetometer (VSM) with the magnetic field applied in-plane. As usually observed, the deposition by sputtering of the magnetic layer leads to the existence of an easy axis of magnetization, as shown in **Figure 3**. The transition point along the easy axis is around 0.86 mT, and the transition point along the easy axis is around 3.8 mT. Note that when Co_{40}–Fe_{40}–B_{20} film is sandwiched between the adhesion layer (Ta) and the protective layer (Pt), its magnetic properties are independent of the substrate considered.

Figure 4 presents an optical microscope image of the device as viewed from the top. The hard axis is parallel to the wave

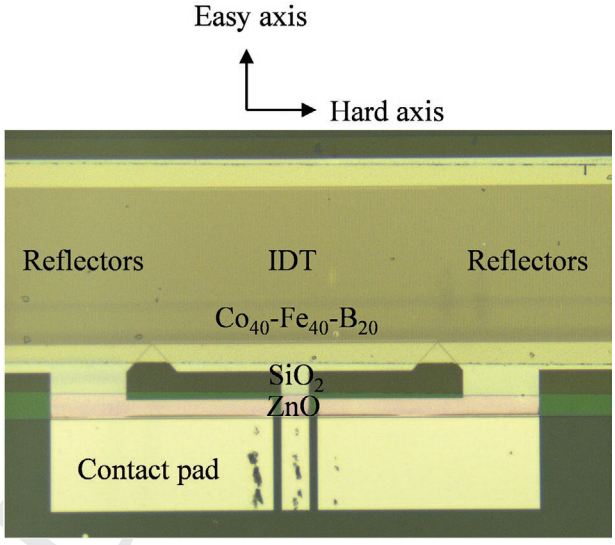

Figure 4. The top view of optical microscope image of the SAW sensor.

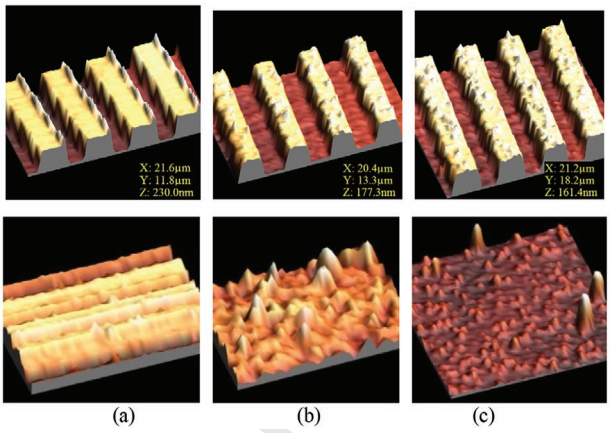

Figure 5. The atomic force microscope of the a) ZnO film, b) SiO_2 film, c) Co–Fe–B film on the device. Top Figures are performed on the top of area with IDTs and bottom ones obtained from area without IDTs.

propagation. The contact pad is not covered by the three functional layers. During the Co_{40}–Fe_{40}–B_{20} film depositing using magnetron sputtering, the gun on which the Co_{40}–Fe_{40}–B_{20} target is fixed includes a magnetron, a strong magnet that increase the sputtering rate of Ar+. The stray field the magnetron makes that the Co_{40}–Fe_{40}–B_{20} layer is deposited under an applied field. This field induces an easy axis of magnetization. The configuration of the stray field in the sputtering is known and fixed. Before deposition of the Co_{40}–Fe_{40}–B_{20} layer, the expectant direction of easy axis is determined, and then the substrate and IDT are oriented in consequence. **Figure 5** illustrates the atomic force microscope (AFM) images produced at different areas (with or without IDTs) and at different stages of successive depositions of the functional films (ZnO, SiO_2, and Co–Fe–B) constituting the multilayer structure. The roughness plays a role in influencing the insulation performance.[31] The RMS roughnesses (R_{RMS}) measured on the top of areas without IDTs are 14.1, 9.0, and 9.9 nm respectively on ZnO, SiO_2, and Co–Fe–B film surfaces. The bumps around edges of IDT probably result from the rough edges of Al electrodes. The bumps diminish as the number of layers increases.

On the top of IDTs areas, measured R_{RMS} values are 8.5, 3.8, and 17.6 nm respectively on ZnO, SiO_2, and Co–Fe–B film surfaces. The SiO_2 layer provides a less rough surface for Co–Fe–B deposition and has an excellent electrical insulation characteristic than ZnO. The SiO_2 layer works as an insulating layer between the Co–Fe–B and the ZnO layers. The combination of this structure therefore leads to a better electrical insulation of the electrodes from the ferromagnetic Co–Fe–B layer and thus a cleaner response from the device.

3. Experiment and Discussion

3.1. Sensor Characterization under Temperatures

The reflection coefficients of the fabricated devices are measured using a Vector Network Analyzer (VNA: Agilent PNA 5230A, Santa Clara, CA) and RF probe station (PM5 Suss MicroTech). A set of GSG probes (GGB-150 μm, Cascade Microtech)

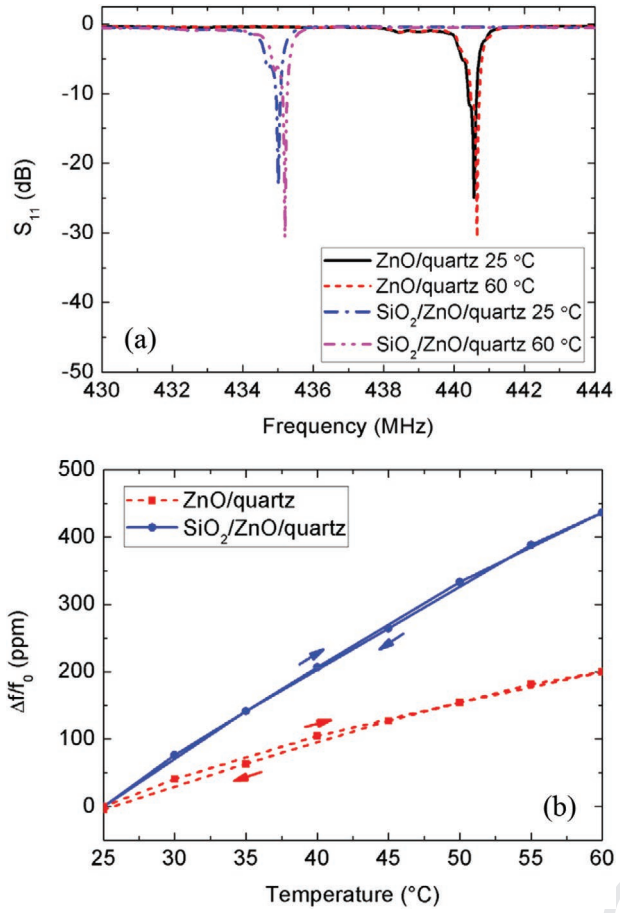

Figure 6. a) The measured S_{11}. b) the relative frequency variations of ZnO/ST+90° -cut quartz and SiO_2/ZnO/ST+90°-cut quartz resonators versus temperature.

connects the device to the VNA. The entire system is calibrated at the end of the probes using a calibration kit to obtain the intrinsic characterization of the sensor by eliminating all the parasitic effects due to the connections and to the elements surrounding the sensor. The thermally controlled chuck of the probe station enables a stable and well controlled temperature variation of up to 60 °C. This allows us to monitor the drift of the resonance frequency with temperature using the VNA.

Figure 6a shows the measured S_{11} at two temperatures. The resonance frequencies measured at room temperature are 440.55 and 434.9 MHz respectively for ZnO/ST+90°-cut quartz and SiO_2/ZnO/ST+90°-cut quartz resonators. The decrease of resonance frequency is due to the low acoustic velocities of ZnO and SiO_2 compared to those of quartz (ST-cut in *X*+90° direction). Figure 6b illustrates the relative frequency variations of Love waves versus temperature. The arrows represent the increase and decrease of temperature. After depositing the SiO_2 film, measured TCF values shift from +10 ppm/°C on ZnO/ST+90°-cut quartz to +17.8 ppm/°C on SiO_2/ZnO/ST+90°-cut quartz due to the positive temperature coefficients of SiO_2.

To study the impedance matching of SAW resonators, the measured Smith charts at two different temperatures for the three studied resonators (Al/quartz, ZnO/Al/quartz, SiO_2/ZnO/Al/quartz) are illustrated in **Figure 7**. It is found that the

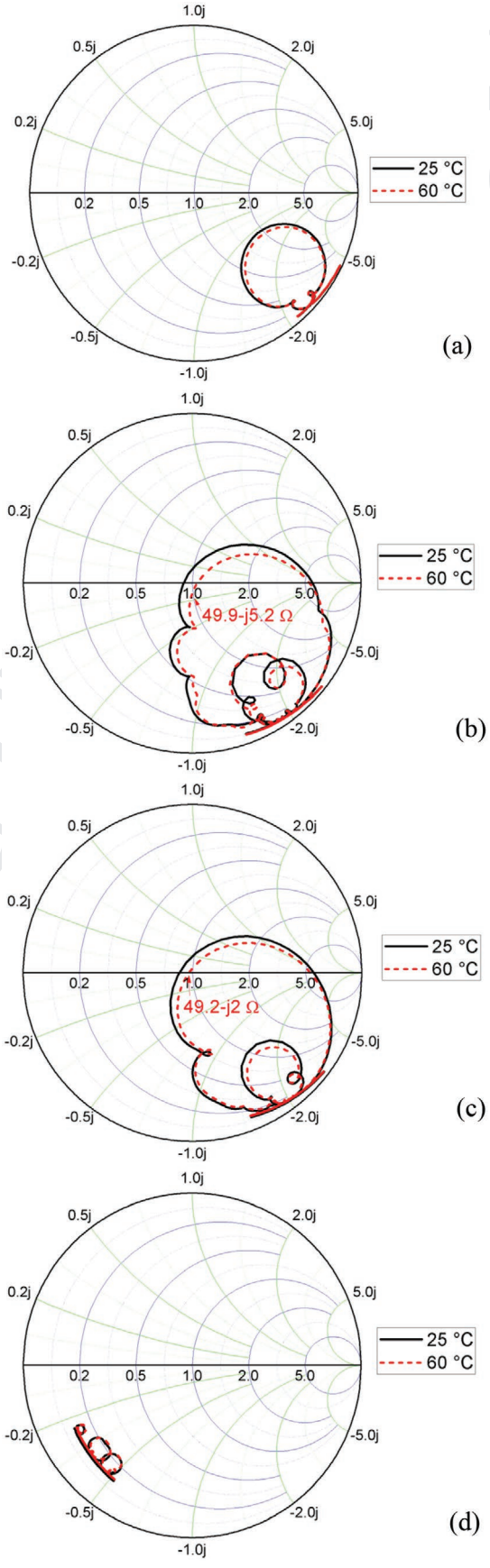

scattering parameters change slightly with temperature which is an advantage in the operation of the sensor in real conditions. As shown in Figure 7a, before the ZnO film deposition, Al/ST+90°-cut quartz resonator has no impedance match to 50 Ω and exhibits a capacitive behavior. After depositing 0.03λ thick ZnO film, the resonance frequency of Love wave mode has been impedance matched to near 50 Ω, as shown in Figure 7b. Depositing a 0.025λ thick SiO_2 film has slight impact on the impedance matching at the resonance frequency in Figure 7c. The quality factor (Q) is extracted from the real part of the resonator admittance $Q = f_r/(2\Delta f_{3dB})$. Δf_{3dB} is the 3dB bandwidth.[32] The Q factor is determined for each intermediate structure and obtained values are: Q = 1860 for Al/quartz; Q = 1300 for ZnO/Al/quartz; Q = 2000 for SiO_2/ZnO/Al/quartz. The different quality factors are related with the damping loss of layers. After the Co–Fe–B film deposition, the impedance curves are at the bottom semicircle of the Smith chart in Figure 7d, confirming the dominance of parasitic capacitance effect. The impedance at the Love wave mode resonance frequency decreases to 10.8–19.4i Ω. A low resistance device is favorable for radiation power by the sensor antenna. The dielectric constant of SiO_2 is lower than that of ZnO. SiO_2 has a better insulating effect than ZnO in this structure.

These parasitic effects could be minimized by increasing the thickness of the insulating layers. This is entirely possible in this structure while maintaining temperature compensation. Indeed, temperature compensation could be achieved only by a film of ZnO as a waveguiding layer. However, the metallic nature of the Co–Fe–B layer makes it a good electrical conductor which generates leakage currents between the IDT fingers through the thin layer of ZnO thus increasing the propagation losses and noise in frequency response of the sensor.[33]

The measured S_{11} of the SAW resonator deposited Co–Fe–B is shown in **Figure 8**a. The base line of S_{11} signal is around –1.7 dB and the amplitude decrease a lot due to the damping loss and parasitic capacitance after depositing the Co–Fe–B film. A part of the electric current flows to the Co–Fe–B film. The wave modes are distinguished from the multiple peaks by observing the shape of the 3D deformation and displacements of the particles in a finite element simulation. The Love wave mode operates at 409.6 MHz and related Q factor of the Love wave mode is 1100. The Rayleigh wave mode is at 328.2 MHz, and the Q factor is 3000.

The frequency–temperature characteristics of the Love wave and Rayleigh wave are illustrated in Figure 8b. As predicted by calculation, the temperature compensation of Love wave mode is achieved well. Indeed, a near zero value of TCF is measured. For the Rayleigh wave mode, the measured TCF value is –37.9 ppm/°C. Thus, this mode is highly sensitive to the temperature and can be used for the temperature measurement. There is also a leaky wave mode at 562.4 MHz, and the related TCF value is –97.4 ppm/°C. However, the Q factor of the leaky wave mode is only 216.

Figure 7. a) The measured Smith chart of Al/ST+90° -cut quartz resonator. b) The Smith chart of ZnO/ST+90° -cut quartz resonator. c) The Smith chart of SiO_2/ZnO/ST+90° -cut quartz resonator. d) The Smith chart of Co–Fe–B/SiO_2/ZnO/ST+90° -cut quartz resonator.

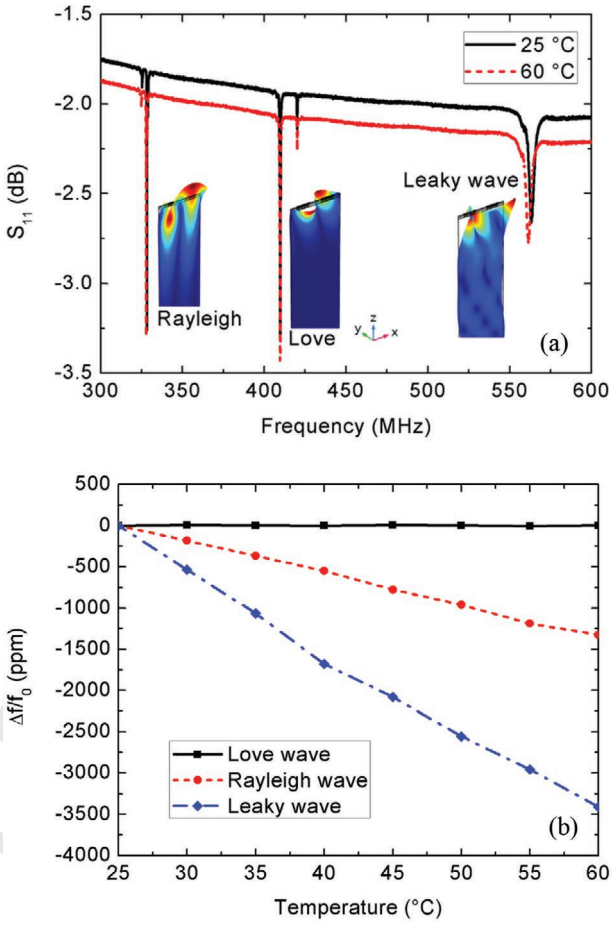

Figure 8. a) Wide band measured S_{11} of Co–Fe–B/SiO_2/ZnO/ST+90° -cut quartz. Resonances related to Rayleigh, Love and leaky waves are observed. b) The frequency-temperature characteristics of wave modes on Co–Fe–B/SiO_2/ZnO/ST+90° -cut quartz.

3.2. Sensor Characterization under Magnetic Fields

The magnetic field measurements of the sensor are made at room temperature using a LakeShore cryogenic probe station (EMPX-HF) connected to a Vector Network Analyzer (VNA: Rohde and Schwartz ZVA67). To avoid any problem of magnetic disturbance, we used nonmagnetic probe head (40 GHz GGB Picoprobes) connected to the VNA via a K-cable. During the measurement, the device is placed between the electromagnets in a vacuum sealed chamber, to ensure a thermally stable and isolated environment. The water-cooled electromagnets are capable of providing a magnetic field up to 600 mT. The influence of temperature on magnetic field sensing is negligible for the temperature compensated Love wave mode at least from room temperature up to 60 °C.

The frequency variations of the fundamental Love wave mode versus the applied magnetic field along the easy axis is measured, as shown in **Figure 9**a. The easy axis is perpendicular to the wave propagation. The sensor is also sensitive in the easy axis. The frequency variation changes from 0 to –865 ppm when the magnetic field increases from 0 to 0.86 mT. However, there is obvious hysteresis when the applied magnetic field is

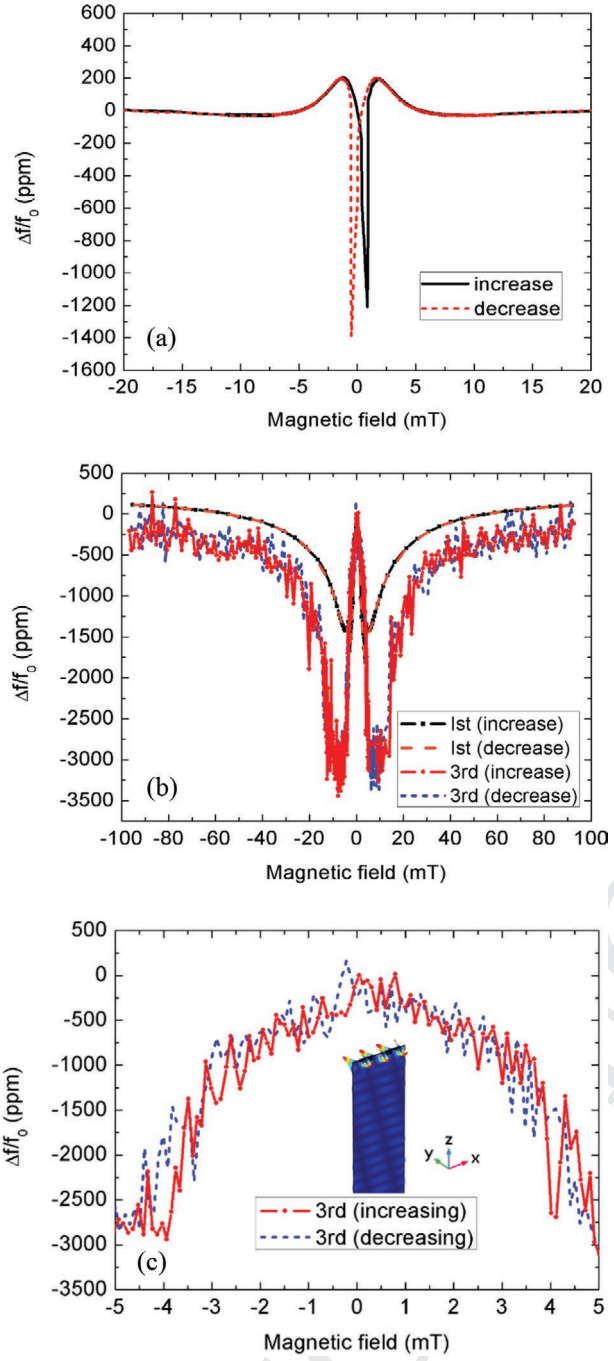

Figure 9. a) The measured frequency variations of the Love wave mode as a function of the applied magnetic field along the easy axis. b) The measured frequency variations of the Love wave mode and c) The zoom-in measured frequency variations of the third-order harmonic Love wave mode as a function of the applied magnetic field along the hard axis.

along the easy axis. Note that hysteresis could be canceled by a micro structuration of the magnetic sensitive layer, such as ferromagnetic strips instead of a full film.[34]

Figure 9b shows the measured magneto-acoustic response of the Love wave versus the intensity of an applied magnetic field between –100 and 100 mT along the hard axis (i.e., parallel to acoustic wave propagation direction). The patterns in Figure 9b

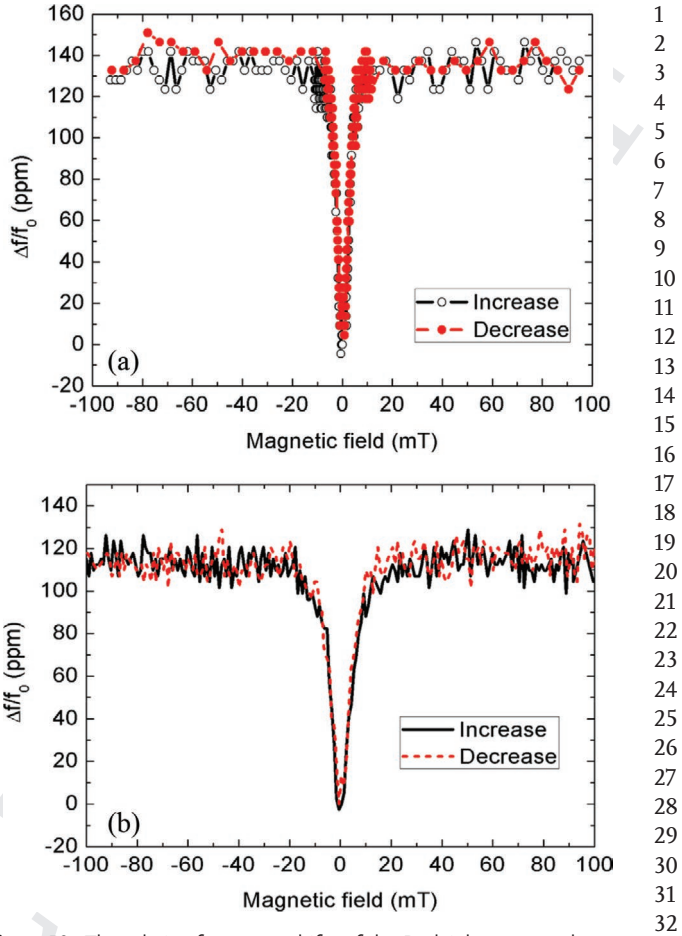

Figure 10. The relative frequency shifts of the Rayleigh wave mode as a function of an applied external magnetic field along the a) easy axis and b) hard axis.

are different from that in Figure 9a due to the magnetoelastic anisotropy and different transition points along the easy and hard axes. Note that in accordance with the deposition process, the perpendicular orientation corresponds to the easy axis of the ferromagnetic film. A relative frequency change of Love wave mode is around –1500 ppm when the applied hard axis magnetic field increases from 0 to 3.8 mT corresponding to a sensitivity of –170.4 kHz m^{-1} T^{-1}. The fundamental Love wave mode has weak hysteresis when the magnetic field direction changes. The produced SAW device has the advantage of exhibiting a resonance peak at 1001 MHz corresponding to the third-order harmonic of the Love wave mode. This peak is also characterized as a function of the applied magnetic field to study the effect of the increase in frequency on the behavior and in particular the sensitivity of the sensor. It is found that the relative magnetic field sensitivity of the third-order harmonic Love wave mode is twice as many as the fundamental Love wave mode. The resonance frequency decreases to the minimum –3113.4 ppm when the applied magnetic field increases from 0 to 5 mT. And the corresponding slope magnetic sensitivity is –621.6 kHz m^{-1} T^{-1}.

The measured frequency-magnetic field characteristics of Rayleigh wave mode from –100 to 100 mT along the easy axis and hard axis are illustrated in **Figure 10**. For the Rayleigh wave mode, a change of 130 ppm is recorded in the magnetic field

Table 1. Comparison of magnetic field sensitivities obtained from various magnetic SAW sensors.

Structure	Magnetic field sensitivity
Fundamental Love wave mode [this work]	170.4 kHz m^{-1} T^{-1}
3rd Love wave mode [this work]	621.6 kHz m^{-1} T^{-1}
FeCoSiB/SiO_2/ST-cut Quartz[28]	504° m^{-1} T^{-1}
FeCoSiB/SiO_2/ST- 90°X Quartz[27]	364.28 kHz m^{-1} T^{-1}
CoFeB/ZnO/Quartz[26]	15.536 kHz m^{-1} T^{-1}
[$TbCo_2$-FeCo]/Y-cut $LiNbO_3$[25]	≈11.2 kHz m^{-1} T^{-1}
[$TbCo_2$-FeCo]/128°-Y cut $LiNbO_3$[24]	2.38 kHz m^{-1} T^{-1}
Ni/ST- 90°X Quartz[23]	≈2.14 kHz m^{-1} T^{-1}
Ni/ZnO/$LiNbO_3$[22]	≈0.112 kHz m^{-1} T^{-1}

range of 0–10 mT along the easy axis corresponding to a sensitivity around 4 kHz m^{-1} T^{-1}. Then, the frequency remains nearly constant when the magnetic field is above 10 mT. When the magnetic field is applied along the hard axis, the relative frequency shift of Rayleigh wave mode is around 110 ppm from 0 to 20 mT corresponding to a sensitivity around 1.8 kHz m^{-1} T^{-1}. The Rayleigh wave mode is insensitive to magnetic fields when the magnetic field is over 20 mT along the hard axis or over 10 mT along the easy axis. It also shows weak hysteresis when the magnetic field direction changes. When the magnetic field is below the saturation field, the temperature is calculated by $T = (f-f_0-S_{mag}\Delta H)/f_0 \cdot TCF+T_0$. T, f, f_0, S_{mag}, ΔH, and T_0 represent temperature, resonance frequency of Rayleigh wave mode at the temperature, resonance frequency of Rayleigh wave mode at room temperature, the slop magnetic field sensitivity of Rayleigh wave mode below the saturation field, magnetic field variation, and room temperature, respectively. In this way, the influence of magnetic field on temperature is compensated for Rayleigh wave mode.

The frequency-magnetic field curve shapes of Love wave and Rayleigh wave modes are different due to ΔE effect. Compared with the Love wave mode, the Rayleigh wave mode is less sensitive to the magnetic field. Therefore, the Rayleigh wave mode can be used for temperature measurement due to its TCF value of −37.9 ppm/°C when the magnetic field is over 10 mT. Thus, a magnetic field and temperature measurements are realized by this dual mode SAW sensor. **Table 1** compares the magnetic field sensitivity of this work with those reported in the literature.[22–28] Note that our structure allows the temperature compensation.

3.3. Wireless Measurement of Electric Current Intensities

This resonance mode is considered in this part to perform dynamic and remote measurement of electric currents in an actual usage scenario. Wireless measurements are done for various field levels. The SAW sensor is tested in a DC electric cable experiment scenario, as shown in **Figure 11**a. An electric current source controls the DC electric current intensities. The SAW sensor is installed on the insulating epoxy resin and is connected to an omni antenna. The schematic diagram of the self-built reader system is shown in Figure 11b.

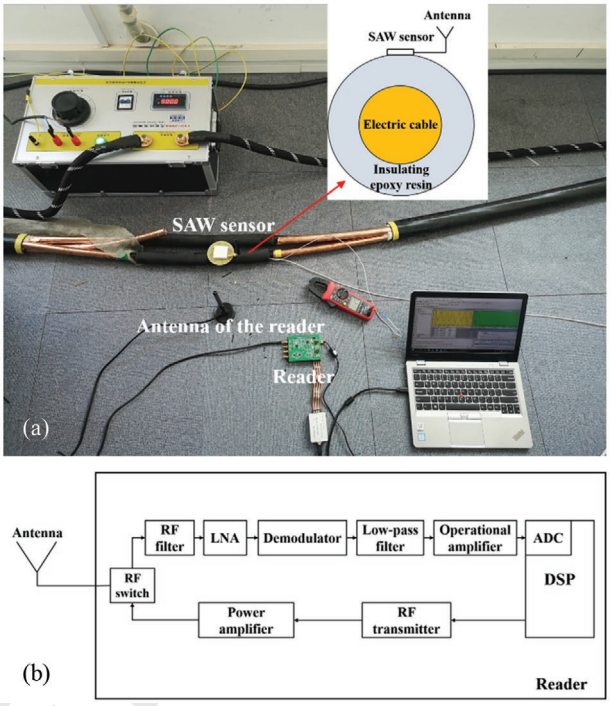

Figure 11. a) The wireless multifunctional SAW sensor experiment scenario for direct electric current. b) Schematic diagram of the self-built reader system.

The self-built reader wirelessly interrogates the SAW sensor through an antenna. The interrogating signals are generated by a DSP controlled RF transmitter. The echo signals from the SAW sensor are demodulated and then time-sampled by the analog-to-digital converter (ADC) in a DSP real-time microcontroller. The sampling rate of the ADC is 11.25 MHz. A high-speed RF switch is used for the transmitter-receiver isolation. The maximum transmitted power of the reader is 25 dBm, and the receiver sensitivity is −90 dBm. The maximum wireless signal transmission distance of the sensor is 30 cm.

The SAW sensor is tested for applied step electric current intensities to study the sensor's dynamic response characteristics. The electric current increases from 0 to 1.5 A with a step of 0.5 A. The magnetic field intensity related to 1 A electric current is about 0.2 mT. Note that if greater field strengths are involved, it is possible to optimize the sensitivity of the sensor by modifying its constituent elements or quite simply by varying the distance between the sensor and the electric cable. **Figure 12**a illustrates the demodulated response sensor signals received by the reader in the time domain.

The low noise amplifier (LNA) of the reader is saturated during the first three periods. It is found that the effective echo signal length is around 10 µs. When the step electric current is applied, the frequency of the sensor decreases suddenly as shown in Figure 12b. The dynamic response time of the SAW sensor is lower than the reader's interrogation cycle of 50 µs. The experiment results indicate that the corresponding theoretical frequency bandwidth of the reader system is 20 kHz.

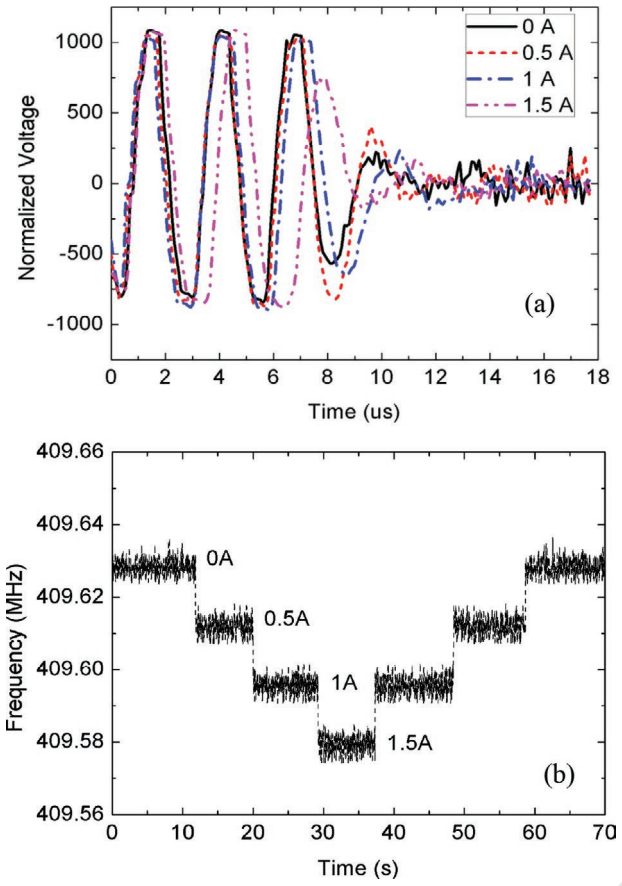

Figure 12. a) Response signals of the Love wave mode for various electric current intensities. b) Measured frequency shifts of the Love wave mode for various electric current intensities.

4. Conclusion

In this paper, a dual mode SAW resonator based on Co_{40}–Fe_{40}–B_{20}/SiO_2/ZnO/quartz multilayered structure operates as a multifunctional sensor. Such a structure combining Love wave and Rayleigh wave allows to measure wirelessly magnetic field intensity and temperature simultaneously and independently. The Rayleigh wave mode with a large TCF value (–37.9 ppm/°C) and a low magnetic field sensitivity is used for temperature measurement. The Love wave mode exhibits a high sensitivity to magnetic field intensity and is insensitive to temperature. The temperature compensation is achieved for this mode by the combination of layers with positive TCF values (quartz and SiO_2) and layers with negative ones (ZnO and Co_{40}–Fe_{40}–B_{20}). The addition of SiO_2 layer brings a flatter surface for Co_{40}–Fe_{40}–B_{20} deposition. The sensor with a slope sensitivity of –170.4 kHz/mT is achieved when considering the fundamental mode of the Love wave operating around 409 MHz and –621.6 kHz m^{-1} T^{-1} when considering its third harmonic operating around 1 GHz. Wireless operation of the sensor is demonstrated by considering the fundamental mode of the Love wave and by measuring the magnetic fields induced by different intensities of electric currents. The proposed structure is beneficial to design reliable hybrid wireless SAW magnetic field and temperature multifunctional sensors.

Acknowledgements

This research was supported by the CAPMAT project ("FEDER-FSE Lorraine et Massif Vosges 2014–2020" and ICEEL). Experiments are carried out at MiNaLor clean-room platform which is partially supported by FEDER and Grand Est Region through the RaNGE project and at IJL Project TUBE-Davm equipment funded by the French PIA project "Lorraine Université d'Excellence" (ANR-15-IDEX-04-LUE).

Conflict of Interest

The authors declare no conflict of interest.

Data Availability Statement

Research data are not shared.

Keywords

dual mode, magnetic field sensor, surface acoustic wave resonator, temperature

Received: July 13, 2021
Revised: September 10, 2021
Published online:

[1] C. Li, T. Ning, X. Wen, J. Li, C. Zhang, C. Zhang, *Opt. Laser Technol.* **2015**, *72*, 104.
[2] W. Wang, Y. Jia, X. Liu, et al., in *Proc. of 2017 IEEE Int. Ultrasonics Symp. (IUS)*, IEEE, xxxx, **2017**, pp. 1–3.
[3] T. Kimura, M. Omura, Y. Kishimoto, H. Kyoya, M. Mimura, H. Okunaga, K. Y. Hashimoto, *Proc. of 2019 IEEE Int. Ultrasonics Symp.*, **2019**, pp 1239–1248.
[4] S. Ballandras, E. Courjon, F. Bernard, et al., *2019 Joint Conf. of the IEEE Int. Frequency Control Sym. and European Frequency and Time Forum (EFTF/IFC)*, IEEE, xxxx **2019**, p. 1–6.
[5] T. M. A. Gronewold, *Anal. Chim. Acta* **2007**, *603*, 119.
[6] J. Hornsteiner, E. Born, G. Fischerauer, et al., *Proc. of the 1998 IEEE Int. Frequency Control Symp.*, xxxx IEEE, xxxx **1998**, pp. 615–620.
[7] S. A. Zhgoon, A. S. Shvetsov, S. A. Sakharov, O. Elmazria, *IEEE Trans. Sonics Ultrason.* **2018**, *65*, 657.
[8] U. Wolff, F. L. Dickert, G. K. Fischerauer, W. Greibl, C. C. W. Ruppel, *IEEE Sens. J.* **2001**, *1*, 4.
[9] C. Floer, S. Hage-Ali, S. Zhgoon, M. Moutaouekkil, F. Bartoli, H. Mishra, S. Mcmurtry, P. Pigeat, T. Aubert, O. Bou Matar, A. Talbi, O. Elmazria, *IEEE Trans. Sonics Ultrason.* **2018**, *65*, 1925.
[10] V. P. Plessky, L. M. Reindl, *IEEE Trans. Sonics Ultrason.* **2010**, *57*, 654.
[11] N. Saldanha, D. Malocha, *IEEE Trans. Sonics Ultrason.* **2012**, *59*, 1750.
[12] C. Floer, S. Hage-Ali, P. Nicolay, H. Chambon, S. Zhgoon, A. Shvetsov, J. Streque, H. M'jahed, O. Elmazria, *IEEE Trans. Sonics Ultrason.* **2019**, *67*, 1267.
[13] W. P. Robbins, A. Young, *IEEE Trans. Sonics Ultrason.* **1985**, *32*, 423.
[14] V. Polewczyk, K. Dumesnil, D. Lacour, M. Moutaouekkil, H. Mjahed, N. Tiercelin, S. Petit Watelot, H. Mishra, Y. Dusch, S. Hage-Ali, O. Elmazria, F. Montaigne, A. Talbi, O. Bou Matar, M. Hehn, *Phys. Rev. Appl.* **2017**, *8*, 024001.
[15] A. Kittmann, C. Müller, P. Durdaut, L. Thormählen, V. Schell, F. Niekiel, F. Lofink, D. Meyners, R. Knöchel, M. Höft, J. Mccord, E. Quandt, *Sens. Actuators, A* **2020**, *311*, 111998.

[16] M. Yamaguchi, K. Hashimoto, H. Kogo, M. Naoe, *IEEE Trans. Magn.* **1980**, *16*, 916.
[17] W. Wang, Y. Jia, X. Xue, Y. Liang, Z. Du, *AIP Adv.* **2018**, *8*, 015134.
[18] P. Smole, W. Ruile, C. Korden, et al., *IEEE Int. Frequency Control Symp. and PDA Exhibition Jointly with the 17th European Frequency and Time Forum, 2003. Proc. of the 2003*, IEEE, xxxx **2003**, pp. 903–906.
[19] W. Li, P. Dhagat, A. Jander, *IEEE Trans. Magn.* **2012**, *48*, 4100.
[20] H. Mishra, M. Hehn, S. Hage-Ali, et al., 2020 IEEE Int. Ultrasonics Symp. (IUS), IEEE, xxxx **2020**, pp. 1.
[21] J. Schmalz, A. Kittmann, P. Durdaut, B. Spetzler, F. Faupel, M. Höft, E. Quandt, M. Gerken, *Sensors* **2020**, *20*, 3421.
[22] M. Elhosni, O. Elmazria, S. Petit-Watelot, L. Bouvot, S. Zhgoon, A. Talbi, M. Hehn, K. A. Aissa, S. Hage-Ali, D. Lacour, F. Sarry, O. Boumatar, *Sens. Actuators, A* **2016**, *240*, 41.
[23] M. Kadota, S. Ito, Y. Ito, T. Hada, K. Okaguchi, *Jpn. J. Appl. Phys.* **2011**, *50*, 07HD07.
[24] H. Mishra, M. Hehn, D. Lacour, O. Elmazria, N. Tiercelin, H. Mjahed, K. Dumesnil, S. Petit Watelot, V. Polewczyk, A. Talbi, O. Bou Matar, S. Hage-Ali, *Smart Mater. Struct.* **2019**, *28*, 12LT01.
[25] H. Zhou, A. Talbi, N. Tiercelin, O. Bou Matar, *Appl. Phys. Lett.* **2014**, *104*, 114101.
[26] H. Mishra, J. Streque, M. Hehn, P. Mengue, H. M'jahed, D. Lacour, K. Dumesnil, S. Petit-Watelot, S. Zhgoon, V. Polewczyk, A. Mazzamurro, A. Talbi, S. Hage-Ali, O. Elmazria, *Smart Mater. Struct.* **2020**, *29*, 045036.
[27] X. Liu, B. Tong, J. Ou-Yang, X. Yang, S. Chen, Y. Zhang, B. Zhu, *Appl. Phys. Lett.* **2018**, *113*, 082402.
[28] A. Kittmann, P. Durdaut, S. Zabel, J. Reermann, J. Schmalz, B. Spetzler, D. Meyners, N. X. Sun, J. Mccord, M. Gerken, G. Schmidt, M. Höft, R. Knöchel, F. Faupel, E. Quandt, *Sci. Rep.* **2018**, *8*, 278.
[29] B. Li, O. Yassine, J. Kosel, *IEEE Sens. J.* **2014**, *15*, 453.
[30] Y. Yang, H. Mishra, T. Han, S. Hage-Ali, M. Hehn, O. Elmazria, *IEEE Trans. Sonics Ultrason.* **2021**, *68*, 2566.
[31] Y. - P. Zhao, G. - C. Wang, T. - M. Lu, G. Palasantzas, J. T.h. M. De Hosson, *Phys. Rev. B* **1999**, *60*, 9157.
[32] K. Y. Hashimoto, *Surface Acoustic Wave Devices in Telecommunications*, Springer-Verlag, Berlin **2000**.
[33] Y. Yang, H. Mishra, P. Mengue, S. Hage-Ali, S. Petit-Watelot, D. Lacour, M. Hehn, H. M'jahed, T. Han, O. Elmazria, *IEEE Sens. J.* **2020**, *20*, 11292.
[34] H. Mishra, M. Hehn, S. Hage-Ali, S. Petit-Watelot, P. W. Mengue, S. Zghoon, H. M'jahed, D. Lacour, O. Elmazria, *Phys. Rev. Appl.* **2020**, *14*.

Q5